Science Bulletin 64 (2019) 391–399

Contents lists available at ScienceDirect

Science Bulletin

journal homepage: www.elsevier.com/locate/scib

Article

Highly efficient and stable solar-powered desalination by tungsten carbide nanoarray film with sandwich wettability

Nana Han [a], Kai Liu [b], Xinping Zhang [c], Meng Wang [c], Pan Du [a], Zhaohui Huang [a], Daojin Zhou [a], Qian Zhang [a], Tengfei Gao [a], Yin Jia [a], Liang Luo [a], Jianjun Wang [b,*], Xiaoming Sun [a,*]

[a] State Key Laboratory of Chemical Resource Engineering, College of Energy, Beijing Advanced Innovation Center for Soft Matter Science and Engineering, Beijing University of Chemical Technology, Beijing 100029, China
[b] Institute of Chemistry, Chinese Academy of Sciences, Beijing 100190, China
[c] Institute of Information Photonics Technology and College of Applied Sciences, Beijing University of Technology, Beijing 100124, China

ARTICLE INFO

Article history:
Received 17 October 2018
Received in revised form 26 December 2018
Accepted 14 February 2019
Available online 7 March 2019

Keywords:
Solar-powered desalination
Tungsten carbide
Nanoarray
Sandwich wettability
Surface plasmon resonance

ABSTRACT

Solar-powered desalination is a promising way to resolve the worldwide water crisis for its low consumption and simple facility. Considering the fragility and aggregations of traditional materials, which may decrease efficiency, we herein introduce a robust tungsten carbide (WC) nanoarray film as a stable and efficient photothermal material, whose absorption is over 97.5% throughout almost the whole solar spectrum range (220–2200 nm) due to nanoarray structure and thus enhanced localized surface plasmon resonance. Besides, for the first time, we modified the film with sandwich wettability. It accelerates evaporation by reducing water's reflection of light, enlarging hydrophobic-hydrophilic boundaries, and depressing heat dissipation. Combining high absorption with unique wettability, the WC nanoarray film offers high solar-to-vapor efficiency of 90.8% and produces drinking water at the rate of (1.06 ± 0.10) kg m^{-2} h^{-1} from man-made seawater and (0.98 ± 0.18) kg m^{-2} h^{-1} from heavy metal sewage under one sun (AM 1.5) while 98% performance remains after 1 h × 100 times' reutilization.

1. Introduction

Water scarcity has become one of the most serious global challenges, while solar-powered desalination (SPD) has raised broad research interests [1–4]. Photothermal materials (PTM) with broad solar absorption have recently attracted significant interest [5], such as carbon materials and plasmonic metal materials [6–17]. However, the absorption of sunlight over 95% throughout large solar spectrum is still challenging [8,10,12] and the long-term stability under illumination is still an issue [18–23]. The more practical problem is that most of the reported SPD materials are usually powders or possess brittle structures that are inadequate for reutilization during desalination [6,8–10,24–27].

Tungsten carbide (WC) nanoparticles are non-toxic [28], and WC is frequently used in hard coating preparations due to its high chemical stability [29] and mechanical durability, with excellent elastic modulus (700 GN m^{-2}) and hardness (2200 Hv) [30]. Furthermore, WC possesses tolerance to laser and distinct local surface plasmon resonance (LSPR) [31]. The LSPR is size-tunable, similar to other plasmonic nanostructures [32]: the plasma response range is broadened as WC particle size decreases from >10 μm to sub-micrometer [31], which makes nanostructured WC a promising candidate for SPD as an ideal PTM.

The development of thermal management strategies through both material and system designs has further improved the overall efficiency [5]. Traditionally, PTMs, such as gold nanoparticles, are dispersed in bulk water. Thus high intensity of light is needed to heat up the whole volume of water for evaporation [25]. In 2014, Chen and co-workers [8] pushed the light-to-vapor efficiency to 65% under one sun by localizing the heat at water surface, and the heat dissipation into bulk water is reduced. In 2016, Zhu and co-workers [24] pushed the efficiency to ~80% by confined 2D water path by blocking heat transfer into bulk water. Another critical factor for evaporation is the surface wettability control on SPD film structures [7,33]. The patterned hydrophobic-hydrophilic surface has been proved favorable for water evaporation by elongating the hydrophobic-hydrophilic boundaries (HHB) [34–37]. However, such HHB effect has never been applied for SPD materials design.

Here, we introduce a robust plasmonic WC nanoarray film as a stable and high efficient PTM, whose absorption is over 97.5% throughout almost the whole solar spectrum range (220–2200 nm), which is among the best reported in literatures

* Corresponding authors.
E-mail addresses: Wangj220@iccas.ac.cn (J. Wang), sunxm@mail.buct.edu.cn (X. Sun).

https://doi.org/10.1016/j.scib.2019.03.008
2095-9273/

(Table S1 online). Furthermore, we introduce a sandwich wettability structure for the first time: a discrete hydrophobic-hydrophilic top layer promotes evaporation with elongated HHBs and reduced sunlight reflection; a discrete hydrophobic-hydrophilic bottom layer can keep a gas cushion to reduce heat dissipation; and a hydrophilic middle layer works as a pump to intake water through capillary force for localized evaporation. Fig. 1 displays the schematics and process flow. The WC nanoarray film with sandwich wettability structure (Sandwich WC) offers high solar-to-vapor efficiency (90.8%) and SPD rate ((1.06 ± 0.10) kg m^{-2} h^{-1}), with cyclic stability among the best reported (Table S2 online) under one sun (AM 1.5). This work should be beneficial to promote wide application of SPD and give inspiration for further optimization of SPD materials to improve SPD efficiency.

2. Materials and methods

2.1. Materials

Tungstic acid was purchased from Aladdin Industrial Corporation. Anhydrous sodium sulfate, hydrogen peroxide, and hydrochloric acid were purchased from Beijing Chemical Works. Polytetrafluoroethylene (PTFE) dispersion, nano graphite, and carbon fiber paper (CFP) were purchased from Alfa Aesar. Melamine was from Tianjin Guang Fu Fine Chemical Research Institute.

2.2. Synthesis of WC nanoarray film

Synthesis of WC nanoarray film is similar to our reported work [38]. First, WO_3 nanoarrays on CFP were synthesized by hydrothermal method. With magnetic stirring, tungstic acid powder (0.625 g) was dissolved in 20 mL 12 wt% hydrogen peroxide solution by heating at 95 °C for 3 h. Then, the solution was transferred into a Teflon reaction kettle with 0.2 g anhydrous sodium sulfate, 115 μL hydrochloric acid, and a piece of 2 cm × 2 cm CFP added in. WO_3 nanoarrays were obtained after being heated for 12 h at 180 °C. Then, WC nanoarray film was got by WO_3 nanoarrays and melamine being heated at 900 °C for 3 h with Ar gas flowing in a tube furnace.

2.3. Materials characterization

The morphologies were examined by JEOL JEM 2100 operating at 200 kV and Zeiss SUPRA-55 operating at 20 kV. X-ray diffraction (XRD) patterns were acquired by Shimadzu XRD-6000 at 10°/min. Mass change is measured by Mettler Toledo ME204E scale connected to the computer by software SerialPortToKeyboard from Mettler Toledo Company. The light source is xenon lamp with CEL-AM1.5 light filter from Zhongjiaojinyuan Company. The light power is controlled by CEL-NP2000 optical power meter from Zhongjiaojinyuan Company. Olympus SZX16 is applied for water droplet imaging. Fluorescence images are captured by a confocal laser scanning microscope (CLSM, Olympus FV 1000) with the samples dyed by Rhodamine B. The wavelength of the exciting and detecting light were 552 and 650 nm. Temperatures are tested by Flir A650SC. ICP tests were carried out by iCAP 6000 Series ICP Spectrometer from Thermo SCIENTIFIC (ppm) and 7700 Series ICP-MS from Agilent Technologies (ppb). Light absorption from 220 to 2,200 nm is measured by UV-3600 UV–VIS-NIR Spectrophotometer from Shimadzu Company.

2.4. Transient spectrum test

Transient spectrums were performed using a femtosecond pump–probe system with a Ti:Sapphire amplifier from Coherent Inc. (Legend Elite), which provides pump pulses centered at about 798 nm with a bandwidth at FWHM of 10 nm, pulse length of about 150 fs, a maximum pulse energy of 1 mJ, and a repetition rate of 1 kHz. A portion of the 800 nm pulses was focused to heavy water with a thickness of 1 mm to produce super-continuum pulses extending from 340 to 1,200 nm, which were used as the probe in the transient absorption (TA) measurements. The pump was focused onto the sample with a diameter of about 0.5 mm and the pump fluence was limited to 650 mJ cm^{-2}, ensuring no damage to the sample. The probe beam was focused into a spot of about 100 μm in diameter within the pump spot on the sample.

2.5. FDTD simulation

All parameters are estimated values. Model for FDTD simulation is shown in Fig. S1 (online), in which the nanobelt is 560, 208, 32 nm in length, width and thickness, separately. The diameter and thickness of nanoparticles on the belts are 16 and 4 nm. Parameters of WC material are as follows: the type is Debye-Drude, conductivity is 126,000 S m^{-1} [39], infinite Freq. relative permittivity is 5.5, static relative permittivity is 5.5 [40], the relaxation time is defined as 340 fs from TA, and density is 15.66 g cm^{-3} from standard PDF card.

2.6. Wettability control

The modification process was performed on 140 °C heating stage when 5 wt% PTFE dispersion was sprayed from 20 cm height onto the sample surfaces. Then the modified samples were heated

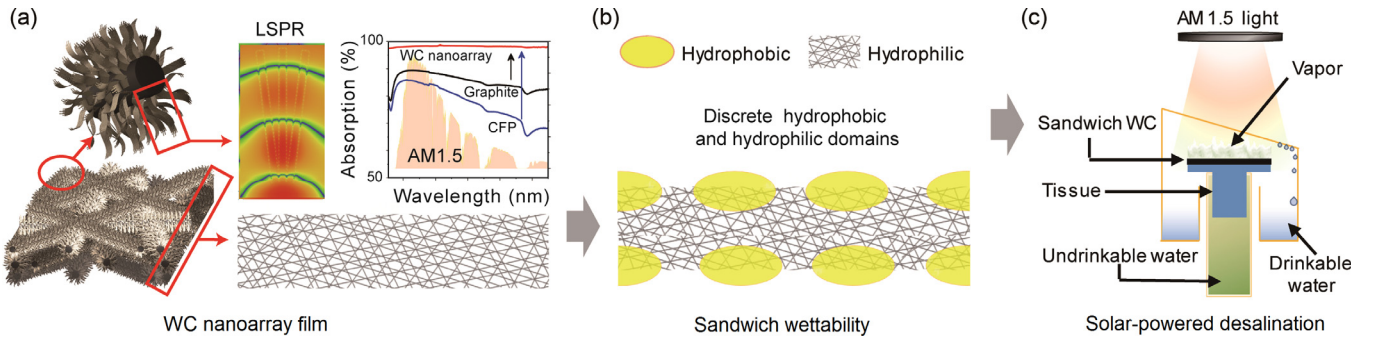

Fig. 1. Schematics and a process flow. (a) WC nanoarray film. The hierarchical nanoarray structure and localized surface plasmon resonance (LSPR) of WC nanoarray film enhance the absorption of light. (b) Sandwich wettability structure. The apparent wettability of the top and bottom layers are both hydrophobic, with discrete micro hydrophobic and hydrophilic domains. The top layer accelerates evaporation by elongating the hydrophobic-hydrophilic boundaries (HHB) and reducing water's reflection of sunlight. The hydrophobic modification with water gates at the bottom reduces heat dissipation to the bulk water by forming a gas film. The middle layer of the film remains hydrophilic to reserve water for localized evaporation. (c) Solar-powered desalination of man-made seawater (MMS) and heavy metal sewage (HMS).

for 30 min at 350 °C to stabilize PTFE. Temperature, flow rate, pressure, height, PTFE concentration and times of spraying were optimized to balance the evaporation with water supply from the bottom surface and realize the best performance.

3. Results and discussion

3.1. Characterizations

Scanning electron microscope (SEM) image in Fig. 2a shows the uniform growth of WC nanoarray on porous CFP substrate. WC nanoarrays are composed of thin WC nanobelts, which are 10–20 nm thick, hundreds of nanometers wide and several micrometers long, as displayed by transmission electron microscopy (TEM) image in Fig. 2b. The nanobelts are composed of WC nanoparticles with size distribution from several nanometers to tens of nanometers (Fig. 2c). This hierarchical structure can trap incident light with multiple reflections. Such strategy has led to enhanced light absorption in silicon nanostructures, carbon nanotubes and other materials [40–42]. In the XRD patterns (Fig. 2d), peaks at 26.4° and 54.5° are features of graphite (PDF No. 41-1487). The peak at 42.5° comes from carbon

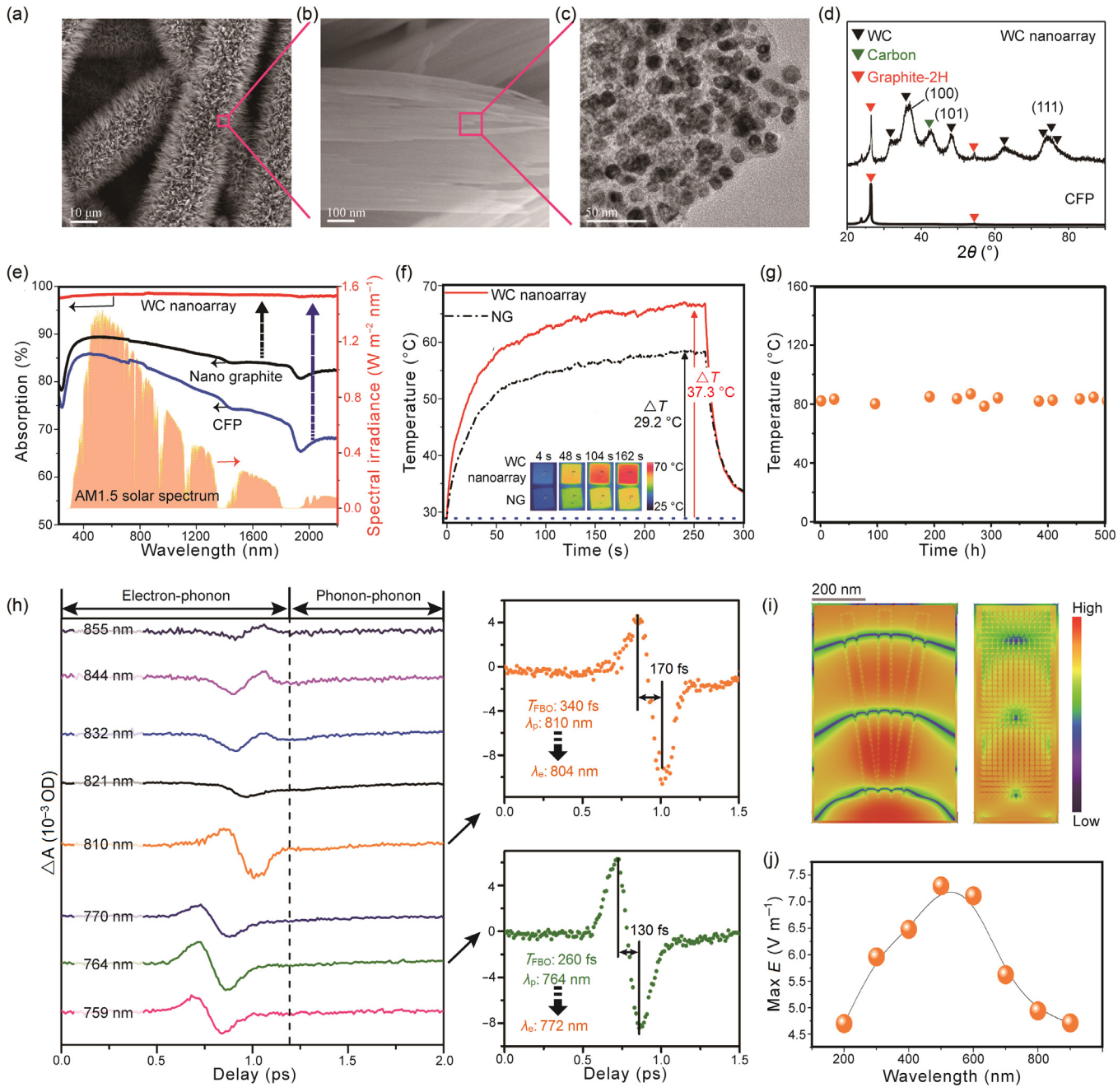

Fig. 2. Characterization of WC nanoarray. (a) SEM of WC nanoarrays on porous CFP. (b) SEM of WC nanobelt. (c) TEM of WC nanobelt composed of WC nanoparticles. (d) XRD data of WC nanoarray film. (e) Light absorption of WC nanoarray film in contrast with CFP and NG. Background is the AM 1.5 solar light spectrum. (f) Solar-thermal response of WC nanoarray film and NG under AM 1.5 light with 260 s illumination. (g) Solar-thermal stability of WC nanoarray film under AM 1.5 light for continuous 500 h. (h) Beat frequency oscillation (BFO) between femtosecond probe photon and WC plasmon resonant electrons. Left is the dynamics of BFO at a series of probe wavelengths (λ_p) from 759 to 855 nm. Right are two enlarged curves at λ_p of 810 and 764 nm. (i) FDTD calculated electric field distribution with 500 nm light input and (j) max electric field intensities with different light input.

(PDF No. 54-0501). All other peaks are indexed to a hexagonal WC phase (PDF No. 51-0939). WC nanoparticles have been proved with LSPR [31], and hierarchical nanostructures with LSPR are proved favorable for the hybridization of LSPR and non-radiative plasmon decay, which can enable efficient and broadband plasmonic absorption [12,43]. The high resolution TEM-energy dispersive spectrometer (HRTEM-EDS) element mapping displayed in Fig. S2 (online) implies that tungsten atoms are mainly distributed at the nanoparticle regions, which are bridged by carbon with slight nitrogen doping. Our previous work [38] verifies in detail about the state of nitrogen doping, which is always used to enhance the hydrophilicity of carbon materials [14,38,44]. Some important works in solar-powered evaporation apply hydrophilicity in accelerating evaporation by favoring water infiltration and transport [14–17].

WC nanoarray film shows high light absorption >97.5% throughout a broad range (220–2,200 nm) in the solar spectrum (Fig. 2e), which is rarely reported for SPD (Table S1 online). The temperature-rising behavior compared with nano graphite (NG) captured by an infrared camera under AM 1.5 light is shown in Fig. 2f and Supplementary Movie 1 (online), where WC nanoarray film displays much faster temperature elevating speed and finally higher temperature. The temperature of WC nanoarray film elevates by 37.3 °C above room temperature, which is 8.1 °C higher than that on NG (29.2 °C above room temperature). In Fig. 2g, the sample shows no significant degradation after continuous 500 h stability test under AM 1.5 light which confirms the reported stability [31]. It is worth noting that, 80 °C in Fig. 2g is the temperature after stabilization.

Transient spectrums in Fig. 2h show the beat frequency oscillation (BFO) process between excited WC electrons and probe pulses (wavelengths from 759 to 855 nm), where fast light responses (0.5–1.2 ps) in every curve indicate plasmon resonance of WC. From the enlarged view of the 810 nm dynamic curve with 340 fs time period (upper right in Fig. 2h), the oscillation wavelength of the excited electrons in WC is calculated to be about 804 nm, which is roughly equal to the wavelength of the pump pulse ((800 ± 5) nm at FWHM). Coverage of oscillation in the pump pulse range suggests that the BFO is resulted from the interference between the pump and probe pulses via the conductive electrons in WC. From the enlarged view of the 764 nm dynamic curve with 260 fs time period (lower right in Fig. 2h) , the oscillation wavelength of the excited electrons in WC is calculated to be 772 nm, which is much lower than the pump pulse. The shift from 804 to 772 nm suggested that the intrinsic plasmonic oscillation of the electrons in the as made WC is much shorter than 800 nm [45]. Detailed analysis and calculation can be found in Supporting Information (online). Similar BFO behavior has been observed on Au nanoparticles, which are known with strong LSP [45].

Hybridization effect of LSP, which enhances light absorption, caused by the hierarchical structure of WC nanoarray could be recognized by the enhanced electric field intensity between nanoparticles and between nanobelts from the FDTD simulation at λ = 500 nm (Fig. 2i). FDTD simulations at various wavelengths (200 to 900 nm) indicate the LSP peak at about 500 nm (Fig. 2j), which is in accordance with the predicted trend from the above BFO curves. The trend indicated by above BFO and FDTD simulation results are verified by absorption spectrum of WC nanobelts suspension in UV–visible range with extinction peak at ~500 nm (Fig. S3 online).

3.2. Wettability enhanced evaporation

Sandwich wettability structure constructed by finite depth PTFE modification is designed to elevate SPD performance of WC nanoarray film. F element distribution (the indicator of PTFE distribution) of the optimized Sandwich WC is shown in Fig. 3a (the side view), where the ~100 μm surface layer (i.e., the bottom and top side) possesses higher F element concentration than the middle layer, indicating more PTFE modification. It should be noted that the distribution of F on the surface is discontinuous, suggesting the spray-coating process induced tiny PTFE dispersion droplets that enable isolated hydrophobic islands. The discrete distribution of F is essential to elongate HHBs at the top surface and build air cushion with water gates at the bottom surface (Fig. S4 online). The hydrophilic middle layer (with low F concentration) can pump up water by capillary force and reserve water for localized evaporation.

Enriched HHBs can also be reflected by the absorption dynamics of water droplets on the modified WC nanoarray film (Fig. 3b). The absorption time on original superhydrophilic WC nanoarray film without PTFE modification is as short as 1 s (Fig. S5 online). The absorption time lasts longer (e.g., 66.40 s) as the surface turns apparently hydrophobic. More importantly, the isolated hydrophobic zones induced by the spray-coating method can help to break the large droplets into smaller ones, which avoids the formation of continual water film and keeps rich HHBs during evaporation (Supplementary Movie 2 online). As shown in Fig. 3b and c, during the earlier stages (Stages 1–3), both the droplet diameters and contact angles (CA) decrease, while the contact line (CL) keeps roughly constant (Fig. 3d). When CAs become too small (too flat), the droplet is cut into two by the hydrophobic lines (Stages 3–4), which induces a jump in CA and splitting of CL (Fig. 3d). The droplet is finally absorbed by the WC nanoarray film with the smallest available diameters in sub-millimeter, which are in accordance with the domain size analysis based on F element distribution (Figs. 3a and S6 (online)).

To further visualize the actual wetting state of the film, we dipped the Sandwich WC into Rhodamin B aqueous solution, which would dye the hydrophilic zones and show red fluorescence under the confocal laser fluorescence microscope (CLFM), as control samples of Superhydrophilic WC and Superhydrophobic WC evidenced (Fig. S7 online). The top view of sandwich WC film is mainly dark with discrete red dots, which are tens of micrometers in diameter (Fig. 3e). These discrete red dots confirm the discrete wettability and imply enriched HHBs of the surface. The side view in Fig. 3e shows the hydrophilicity of the middle layer, where the dark areas in the side view are mainly caused by roughness (Supplementary Movie 3 online).

The sandwich wettability, as fully evidenced by the droplet absorption dynamics and CLFM, enriches the HHBs and keeps water in the middle layer for localized evaporation, and finally enhances the water evaporation performance (Fig. 3f). Because the evaporation rates in Fig. 3f were measured in open air, the value on bare water surface is higher than some reported values [9,11,24] due to the low RH in the environment (11%, 25 °C). Besides NG and blank water, a superhydrophilic (without PTFE modification) and a superhydrophobic sample were also made and used as the control. Their evaporation rates to the air in open circumstances at 25 °C and 11% relative humidity (RH) are measured by the setup in Fig. S8 (online), where a tissue is used to support and pump up water to the sample on it. The tissue helps reducing heat dissipation into the bulk water and pumping water to the films [24]. All three WC nanoarray films show better performance than NG, which confirms the superiority of the WC nanoarray material. As expected, Sandwich WC shows the best performance at an evaporation rate of (2.80 ± 0.02) kg m^{-2} h^{-1}, which is 22%, 34%, 53%, and 131% higher than superhydrophilic WC, superhydrophobic WC, NG and blank water. The boosted performance of Sandwich WC over superhydrophilic and superhydrophobic samples confirms the superiority of the sandwich wettability structure.

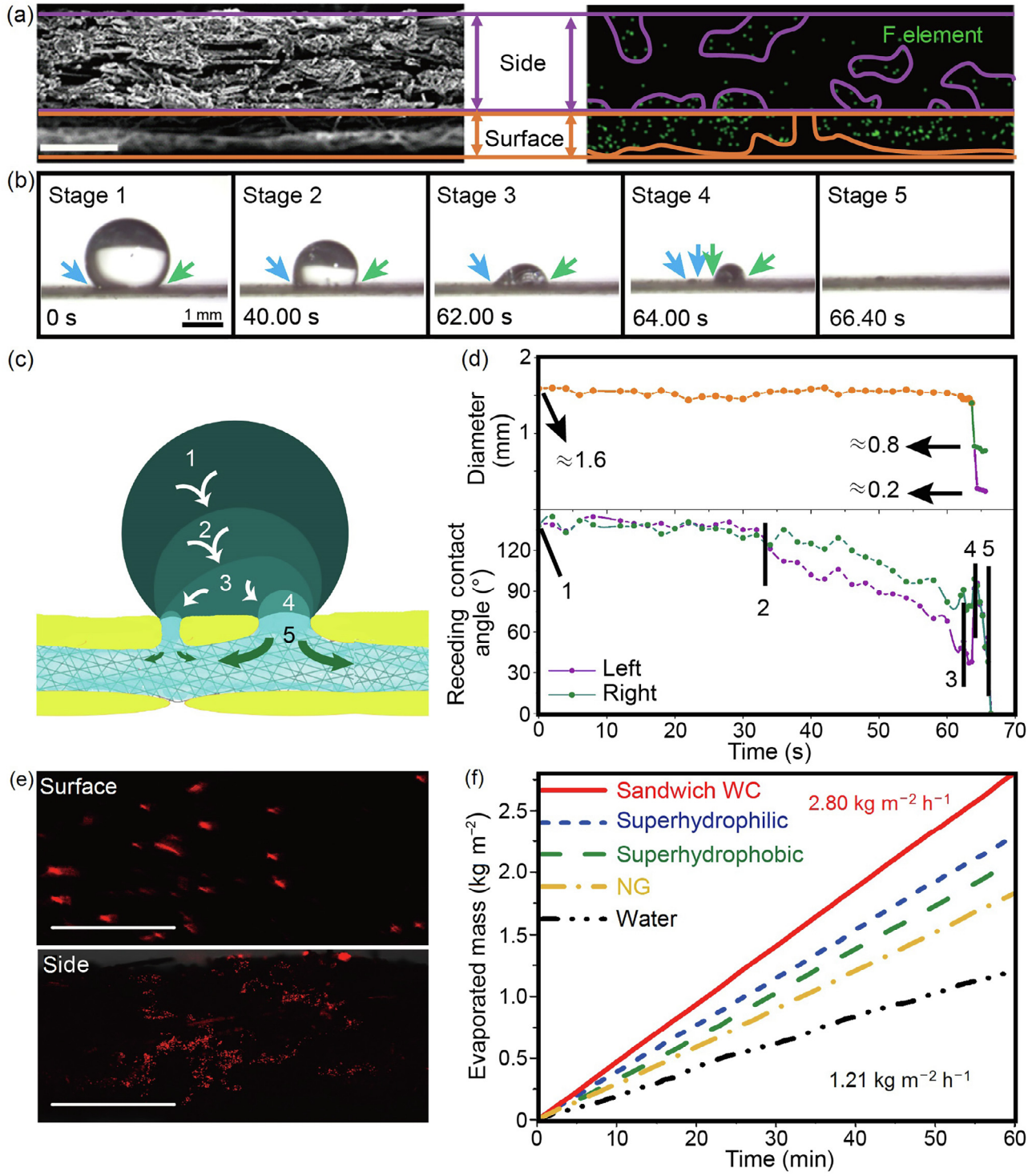

Fig. 3. Wettability enhanced evaporation. (a) SEM of the side view of Sandwich WC and the corresponding EDS mapping of F element distribution. Scale bars: 200 μm. (b) Processes when a water droplet is absorbed by Sandwich WC and the according schematic diagram (c), contact line diameter changes and receding contact angle changes (d). (e) CLFM images of sandwich WC nanoarray film which is dyed by Rhodamin B aqueous solution. Red parts imply hydrophilic domains. Scale bars: 250 μm. (f) Solar-powered water evaporation performance.

The evaporation rate on Sandwich WC outperforms most reported works [6–9,24,46]. To further estimate the solar to vapor efficiency of the material more precisely, the effect of RH [47] and air convection are reduced by evaporation test in a quasi-closed system (Fig. S9 online): when the evaporation occurs, the air in the system is saturated with vapor soon. As the control, an opened system test was carried out with the cover remained on the top (Fig. S10 online) under the same illumination. The evaporation rate in the quasi-closed system ($(1.15 \pm 0.03)\ kg\ m^{-2}\ h^{-1}$) is about 51.6%±0.8% of that in an open system ($(2.24 \pm 0.02)\ kg\ m^{-2}\ h^{-1}$) (Fig. S11 online). This large difference demonstrates the strong effect of air convection and low humidity in evaporation, that it is important to control the environment or at least offer description of the state of environment in studies about solar-powered evaporation in the open air. Assuming that this ratio is the same when Sandwich WC is directly under 1.5 AM light without a cover

on the top, the evaporation rate in a quasi-closed system of Sandwich WC would be (1.45 ± 0.03) kg m^{-2} h^{-1}. When the latent heat of water evaporation (≈2,260 kJ kg^{-1}) is applied to calculate the solar-to-saturated vapor efficiency [8], the efficiency of Sandwich WC is about 90.8%, which is among the best results reported (Table S2 online).

3.3. Mechanism verification of wettability effect

Fig. 4a shows the working state contrast between Sandwich WC and the superhydrophilic sample. The middle layer is remained superhydrophilic to pump up water through the bottom water gates and reserve water for localized heating and evaporation. Combining the advantages of the high heat conductivity of WC (84.02 W mK^{-1}) [30] and foam-like structure [48], the middle layer can transfer heat to the confined water immediately. Otherwise, if the middle layer is hydrophobic (the superhydrophobic sample), there should not be enough water for localized heating and evaporation. So, finite depth PTFE modification (i.e., roughly 1/4 of total film thickness) is critical for the design.

The discrete wettability on the top surface has two advantages (Fig. 4a). First, the discrete hydrophilic and hydrophobic domains elongate the HHBs, which are reported favorable to evaporation [34,35,49]. Second, the reflection by water film on superhydrophilic sample is reduced on Sandwich WC (Fig. 4b). This indicates that the absorbance of a "black" material might be very different in air or on water when they are applied to SPD. As shown in Fig. 4b, wide range of lights are reflected to some extent on the superhydrophilic sample when it changes from dry to wet. In contrast, there is no much difference between the dry and wet Sandwich WC.

The bottom surface of Sandwich WC is designed to reduce heat dissipation to the bulk water [6,8,9,50]. Fig. 4c shows the final spatial temperature distribution near the water surface with WC film on top of a water-saturated-tissue-paper (2-dimensional water path [24]) under the light. The Janus sample without bottom air cushion but with the same hydrophobic surface was used as the control sample to Sandwich WC from the side view. Fig. 4c illustrates a relatively uniform temperature distribution underneath the WC film. In contrast, Fig. 4d shows a much more localized high-temperature zone of Sandwich WC under the light. C_1 and C_2 points in Fig. 4c and d refer to the central point of films and the film/water interface. The larger temperature difference between C_1 and C_2 in Fig. 4d than in Fig. 4c verifies that the hydrophobic bottom of Sandwich WC reduces heat dissipation to the water underneath, as drawn in Fig. 4a.

3.4. Desalination performance

Fig. 5 shows the desalination performance of Sandwich WC. All tests are measured under AM 1.5 light. The evaporation of 3.5 wt%, 17.5 wt% and saturated NaCl solution to the open air are measured by the setup in Fig. S8 (online). 3.5 wt% is the average salt content of seawater, whose evaporation rate is about 2.4 kg $m^{-2}h^{-1}$ (Fig. 5a). The decreased evaporation rate of 17.5 wt% and the saturated NaCl solution may be caused by the decreased chemical potential of water in the solution and the deposited NaCl crystals on the surface of the film. This trend in evaporation rate implies that drying up a bottle of saline water for desalination is not as efficient as distilling slowly flowing saline water with a constant low salt concentration and washing and reutilization is inevitable during desalination. Fig. 5b shows the mass of collected purified water

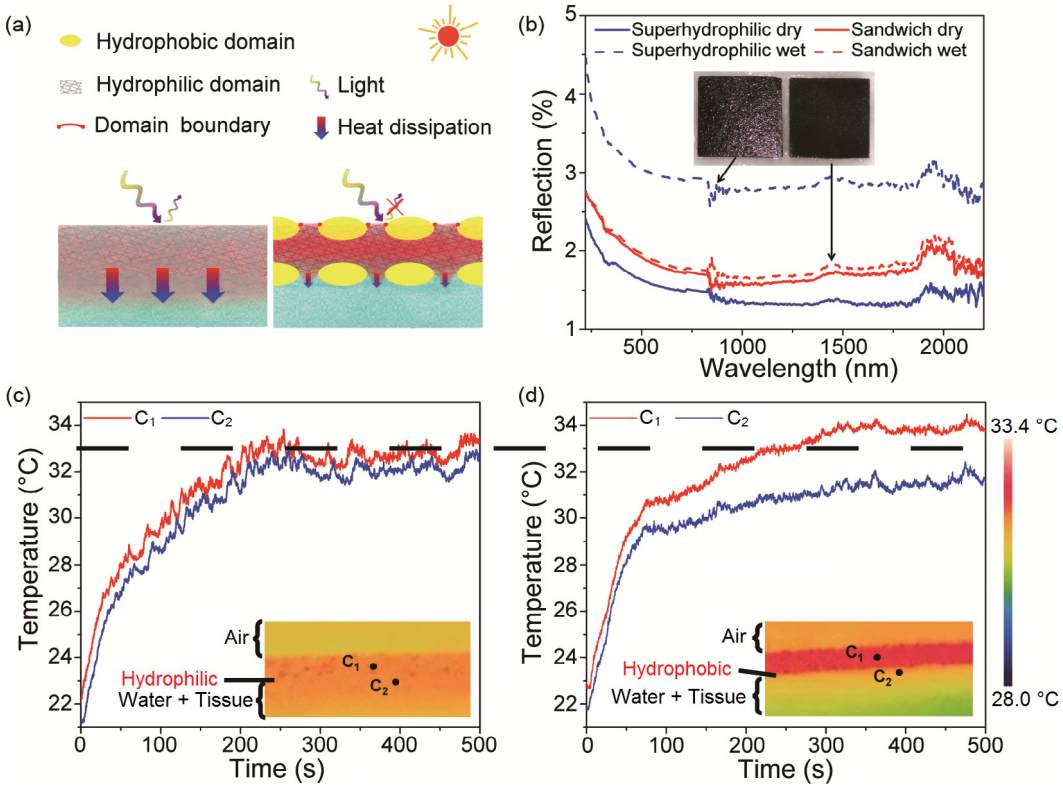

Fig. 4. Mechanism of wettability effect. (a) Schematics of the effect of sandwich wettability structure. The top layer is designed to elongate the HHBs and reduce water reflection of light on the surface. The bottom layer is designed to reduce heat dissipation. The middle layer is remained hydrophilic to pump up water through the bottom water gates and reserve water for heating and evaporation. (b) Reflection curves of Superhydrophilic WC and Sandwich WC when they are dry or wet, which confirms the superiority of the wettability design on the top layer. (c) and (d) show the temperature-rise processes from the side views of a Janus sample (only the top surface is modified with PTFE) and Sandwich WC on water saturated tissues.

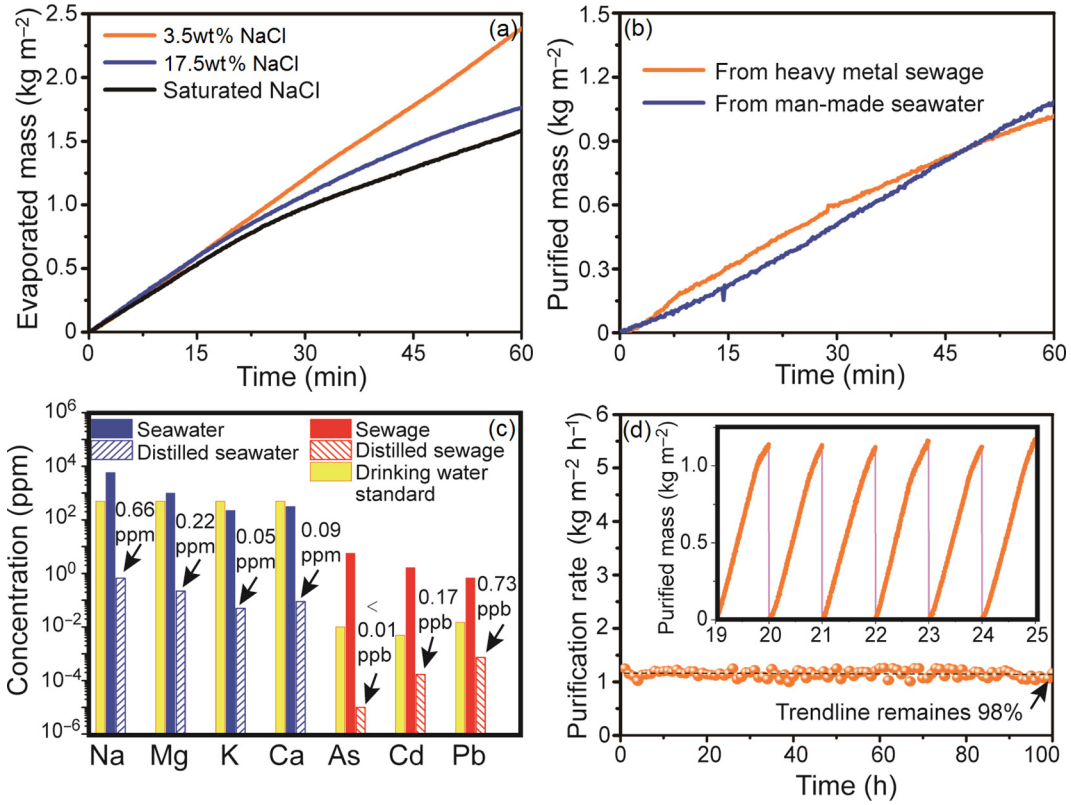

Fig. 5. (Color online) Desalination performance of the sandwich sample. (a) Evaporation of 3.5 wt%, 17.5 wt% and saturated NaCl solution to the open air. 3.5 wt% is the average salt content of seawater. (b) Collected purified water distilled from man-made seawater (MMS) and HMS. (c) Content of the MMS and HMS before and after desalination. (d) Cyclic stability test. Illumination for all tests is AM 1.5.

distilled from man-made seawater (MMS) and heavy metal sewage (HMS) by the setup shown in Fig. S12 (online). The rates of distilled water production are (1.06 ± 0.10) kg m^{-2} h^{-1} from MMS and (0.98 ± 0.18) kg m^{-2} h^{-1} from HMS under normal sunlight.

Fig. 5c shows the salt content before and after MMS and HMS are distilled. Na, Mg, K, Ca contents are all below 1 ppm, which is approximately three orders of magnitude below the drinking water standards defined by the World Health Organization (1‰) and the US Environmental Protection Agency (0.5‰) [10]. As, Cd, Pb contents are all below the maximum contaminant level of drinking water set by the National Primary Drinking Water Regulations of America.

With continuously hours of desalination from 3.5 wt% NaCl solution, obvious deposition of NaCl cystals would appear at the surface, as shown in Fig. S13 (online). The NaCl crystals could be washed out by the original 3.5 wt% NaCl solution, and this process doesn't affect the performance much, as Fig. S13 (online) shows. So, for Sandwich WC, washing the sample after each hour's desalination (which can be realized easily by automation control in industrial) to keep the evaporation rate at a high level is an efficient way to make the best use of solar energy. Fig. 5d shows the 1 h × 100 cycles distillation stability test of 3.5 wt% NaCl solution when the sample was rinsed by saline water and reused for each cycle. The production rate of purified water is around 1.1 kg m^{-2}h^{-1} with 2% decrease at the end of the stability test, which is among the best cyclic stability reported (Table S2).

4. Conclusion

In this work, non-toxic WC is recommended for SPD for the first time. Nanoarray structure and LSPR accelerate WC's absorption to over 97.5% throughout a large range in the solar spectrum. High elastic modulus, hardness, chemical stability and tolerance to laser enable WC a robust plasmonic solar-thermal material, which remains almost the same after 500 h illumination. With effective sandwich wettability structure, solar-to-vapor efficiency is accelerated to 90.8% by reducing water's reflection of light at working state, enlarging the hydrophobic-hydrophilic boundaries, and depressing heat dissipation at the same time. As a result, the Sandwich WC film produces drinking water at a high rate from man-made seawater and heavy metal sewage under normal sunlight (AM 1.5) with outstanding cyclic stability. This system still has potentials for further improvement, for example, if the current simple desalination system could combine with smart water collecting systems [51], the desalination efficiency will be further improved. The material and wettability innovation should give inspiration for further improving solar power desalination efficiency.

Conflict of interest

The authors declare that they have no conflict of interest.

Acknowledgments

Thanks to Beijing Laboratory of Biomedical Materials, Beijing University of Chemical Technology for the help in laser confocal fluorescence microscopy characterization. This work was supported by the National Natural Science Foundation of China (21676022), the National Key Research and Development Program of China (2016YFF0204402), the Program for Changjiang Scholars and Innovative Research Team in the University (IRT1205), the Fundamental Research Funds for the Central Universities, the Long-Term Subsidy Mechanism from the Ministry of Finance and the Ministry of Education of PRC.

Author contributions

Xiaoming Sun, Jianjun Wang, Nana Han and Kai Liu designed the research; Nana Han performed the research; Xinping Zhang, Liang Luo and Meng Wang gave advice and performed the transient spectral measurement; Pan Du performed the FDTD calculation; Zhaohui Huang performed the laser confocal fluorescence microscopy characterization; Qian Zhang, Tengfei Gao, Yin Jia, and Daojin Zhou offered help for ICP, SEM, TEM, and XRD, respectively; Nana Han wrote the paper; Xiaoming Sun, Jianjun Wang, Xinping Zhang, Nana Han and Kai Liu revised the paper.

Appendix A. Supplementary data

Supplementary data to this article can be found online at https://doi.org/10.1016/j.scib.2019.03.008.

References

[1] Voeroesmarty CJ, McIntyre PB, Gessner MO, et al. Global threats to human water security and river biodiversity. Nature 2010;467:555–61.
[2] Liu J, Yang W. Water sustainability for china and beyond. Science 2012;337:649–50.
[3] Gleick PH, Palaniappan M. Peak water limits to freshwater withdrawal and use. Proc Natl Acad Sci USA 2010;107:11155–62.
[4] Tao P, Ni G, Song C, et al. Solar-driven interfacial evaporation. Nat Energy 2018;3:1031–41.
[5] Gao M, Zhu L, Peh CK, et al. Solar absorber material and system designs for photothermal water vaporization towards clean water and energy production. Energy Environ Sci 2019;12:841–64.
[6] Hu X, Xu W, Zhou L, et al. Tailoring graphene oxide-based aerogels for efficient solar steam generation under one sun. Adv Mater 2017;29:1604031.
[7] Li X, Li J, Lu J, et al. Enhancement of interfacial solar vapor generation by environmental energy. Joule 2018;2:1331–8.
[8] Ghasemi H, Ni G, Marconnet AM, et al. Solar steam generation by heat localization. Nat Commun 2014;5:4449.
[9] Zhang L, Tang B, Wu J, et al. Hydrophobic light-to-heat conversion membranes with self-healing ability for interfacial solar heating. Adv Mater 2015;27:4889–94.
[10] Zhao F, Zhou X, Shi Y, et al. Highly efficient solar vapour generation via hierarchically nanostructured gels. Nat Nanotechnol 2018;13:489–96.
[11] Bae K, Kang G, Cho SK, et al. Flexible thin-film black gold membranes with ultrabroadband plasmonic nanofocusing for efficient solar vapour generation. Nat Commun 2015;6:10103.
[12] Zhou L, Tan Y, Wang J, et al. 3D self-assembly of aluminium nanoparticles for plasmon-enhanced solar desalination. Nat Photon 2016;10:393.
[13] Zhou X, Zhao F, Guo Y, et al. A hydrogel-based antifouling solar evaporator for highly efficient water desalination. Energy Environ Sci 2018;11:1985–92.
[14] Xu J, Xu F, Qian M, et al. Copper nanodot-embedded graphene urchins of nearly full-spectrum solar absorption and extraordinary solar desalination. Nano Energy 2018;53:425–31.
[15] Tao F, Zhang Y, Cao S, et al. CuS nanoflowers/semipermeable collodion membrane composite for high-efficiency solar vapor generation. Mater Today Energy 2018;9:285–94.
[16] Xu N, Hu X, Xu W, et al. Mushrooms as efficient solar steam-generation devices. Adv Mater 2017;29:1606762.
[17] Li J, Du M, Lv G, et al. Interfacial solar steam generation enables fast-responsive, energy-efficient, and low-cost off-grid sterilization. Adv Mater 2018;30:1805159.
[18] Link S, Burda C, Nikoobakht B, et al. How long does it take to melt a gold nanorod?: A femtosecond pump–probe absorption spectroscopic study. Chem Phys Lett 1999;315:12–8.
[19] Link S, Burda C, Mohamed MB, et al. Laser photothermal melting and fragmentation of gold nanorods: energy and laser pulse-width dependence. J Phys Chem A 1999;103:1165–70.
[20] Yavuz MS, Cheng Y, Chen J, et al. Gold nanocages covered by smart polymers for controlled release with near-infrared light. Nat Mater 2009;8:935–9.
[21] Huang X, Tang S, Liu B, et al. Enhancing the photothermal stability of plasmonic metal nanoplates by a core-shell architecture. Adv Mater 2011;23:3420–5.
[22] Li J, Han J, Xu T, et al. Coating urchinlike gold nanoparticles with polypyrrole yhin shells to produce photothermal agents with high stability and photothermal transduction efficiency. Langmuir 2013;29:7102–10.
[23] Liu J, Kan C, Cong B, et al. Plasmonic property and stability of core-shell Au@SiO_2 nanostructures. Plasmonics 2014;9:1007–14.
[24] Li X, Xu W, Tang M, et al. Graphene oxide-based efficient and scalable solar desalination under one sun with a confined 2D water path. Proc Natl Acad Sci USA 2016;113:13953–8.
[25] Neumann O, Urban AS, Day J, et al. Solar vapor generation enabled by nanoparticles. ACS Nano 2013;7:42–9.
[26] Zhu G, Xu J, Zhao W, et al. Constructing black titania with unique nanocage structure for solar desalination. ACS Appl Mater Interfaces 2016;8:31716–21.
[27] Li R, Zhang L, Shi L, et al. Mxene Ti_3C_2: an effective 2D light-to-heat conversion material. ACS Nano 2017;11:3752–9.
[28] Bastian S, Busch W, Kuehnel D, et al. Toxicity of tungsten carbide and cobalt-doped tungsten carbide nanoparticles in mammalian cells in vitro. Environ Health Perspect 2009;117:530–6.
[29] Li N, Yan Y, Xia BY, et al. Novel tungsten carbide nanorods: an intrinsic peroxidase mimetic with high activity and stability in aqueous and organic solvents. Biosens Bioelectron 2014;54:521–7.
[30] Hoffmann P, Galindo H, Zambrano G, et al. FTIR studies of tungsten carbide in bulk material and thin film samples. Mater Charact 2003;50:255–9.
[31] Zhang X, Wang H, Wang M, et al. Ultrafast particle-plasmon enhancement by energy-band modification in nanostructured tungsten carbide. Opt Express 2016;24:22730–40.
[32] Yadgarov L, Choi CL, Sedova A, et al. Dependence of the absorption and optical surface plasmon scattering of MoS_2 nanoparticles on aspect ratio, size, and media. ACS Nano 2014;8:3575–83.
[33] Yu S, Zhang Y, Duan H, et al. The impact of surface chemistry on the performance of localized solar-driven evaporation system. Sci Rep 2015;5:13600.
[34] Wan R, Wang C, Lei X, et al. Enhancement of water evaporation on solid surfaces with nanoscale hydrophobic-hydrophilic patterns. Phys Rev Lett 2015;115:195901.
[35] Wan R, Shi G. Accelerated evaporation of water on graphene oxide. Phys Chem Chem Phys 2017;19:8843–7.
[36] He M, Liao D, Qiu H. Multicomponent droplet evaporation on chemical micro-patterned surfaces. Sci Rep 2017;7:41897.
[37] Diddens C, Tan H, Lv P, et al. Evaporating pure, binary and ternary droplets: thermal effects and axial symmetry breaking. J Fluid Mech 2017;823:470–97.
[38] Han N, Yang KR, Lu Z, et al. Nitrogen-doped tungsten carbide nanoarray as an efficient bifunctional electrocatalyst for water splitting in acid. Nat Commun 2018;9:924.
[39] Pawbake A, Waykar R, Jadhavar A, et al. Wide band gap and conducting tungsten carbide(WC) thin films prepared by hot wire chemical vapor deposition (HW-CVD) method. Mater Lett 2016;183:315–7.
[40] Mehmood U, Al-Sulaiman FA, Yilbas BS, et al. Superhydrophobic surfaces with antireflection properties for solar applications: a critical review. Sol Energy Mater Sol Cells 2016;157:604–23.
[41] Huang YF, Chattopadhyay S, Jen YJ, et al. Improved broadband and quasi-omnidirectional anti-reflection properties with biomimetic silicon nanostructures. Nat Nanotechnol 2007;2:770–4.
[42] Mizuno K, Ishii J, Kishida H, et al. A black body absorber from vertically aligned single-walled carbon nanotubes. Proc Natl Acad Sci USA 2009;106:6044–7.
[43] Cheng CW, Sie EJ, Liu B, et al. Surface plasmon enhanced band edge luminescence of ZnO nanorods by capping Au nanoparticles. Appl Phys Lett 2010;96:071107.
[44] Tian W, Wang C, Chen R, et al. Aligned n-doped carbon nanotube bundles with interconnected hierarchical structure as an efficient bi-functional oxygen electrocatalyst. RSC Adv 2018;8:26004–10.
[45] Zhang X, He J, Wang Y, et al. Terahertz beat oscillation of plasmonic electrons interacting with femtosecond light pulses. Sci Rep 2016;6:18902.
[46] Zeng Y, Yao J, Horri BA, et al. Solar evaporation enhancement using floating light-absorbing magnetic particles. Energy Environ Sci 2011;4:4074–8.
[47] Liu CJ, Bonaccurso E, Butt HJ. Evaporation of sessile water/ethanol drops in a controlled environment. Phys Chem Chem Phys 2008;10:7150–7.
[48] Boomsma K, Poulikakos D, Zwick F. Metal foams as compact high performance heat exchangers. Mech Mater 2003;35:1161–76.
[49] Lee M, Lee D, Jung N, et al. Evaporation of water droplets from hydrophobic and hydrophilic nanoporous microcantilevers. Appl Phys Lett 2011;98:013107.
[50] Ni G, Li G, Boriskina SV, et al. Steam generation under one sun enabled by a floating structure with thermal concentration. Nat Energy 2016;1:16126.
[51] Chen Y, Wang L, Xue Y, et al. Bioinspired spindle-knotted fibers with a strong water-collecting ability from a humid environment. Soft Matter 2012;8:11450–4.

Nana Han is now pursuing her Ph.D. degree under the supervision of Prof. Xiaoming Sun at the State Key Laboratory of Chemical Resource Engineering, College of Energy, Beijing University of Chemical Technology. Her current researches mainly relate to synthesises of inorganic nanostructures and their applications in energy conversion and storage.

Jianjun Wang obtained his Ph.D. degree at Max-Planck Institute for Polymer Research and the University of Mainz (Germany) in 2006. After seven months of post-doctoral research, he became a project leader at Max-Planck Institute for Polymer Research. Since 2010, he has been a professor at the Institute of Chemistry, Chinese Academy of Sciences. His current research interest is anti-icing materials.

Xiaoming Sun achieved his B.S. and Ph.D. degree at Tsinghua University at 2000 and 2005, respectively. He worked in Stanford as a postdoc from 2005. He joined Beijing University of Chemical Technology from 2008. His current research interest mainly focuses on the synthesis and separation of nanomaterials, to improve the energy related electrocatalysis process by tailoring the compositions, surface wettability, and micro-/nano-structures.